Catalysis Science & Technology

Accepted Manuscript

ROYAL SOCIETY OF CHEMISTRY

www.rsc.org/catalysis

Journal Name

RSCPublishing

ARTICLE

A facile strategy for enhancing FeCu bimetallic promotion for catalytic phenol oxidation

Cite this: DOI: 10.1039/xoxxoooooox

Lei Luo[a], Chengyi Dai[a], Anfeng Zhang[a], Junhu Wang[b], Min Liu[a], Chunshan Song[ac]* and Xinwen Guo[a]*

Received ooth January 2012,
Accepted ooth January 2012

DOI: 10.1039/xoxxoooooox

www.rsc.org/

The mesoporous ZSM-5 zeolite obtained from alkaline treatment was found to be a superior support of bimetallic FeCu, minimizing the nanoparticle size, enhancing the bimetallic interaction, and promoting catalytic oxidation of phenol. The physicochemical characteristics of the as-prepared Fe_xCu_y/ZSM-5 samples were evaluated by XRD, TEM, Ar adsorption, H_2-TPR, and ^{57}Fe Mossbauer spectroscopy which revealed strong bimetallic interaction. Meanwhile, phenol oxidation was applied as a probe reaction under mild conditions. Supported FeCu bimetallic oxides on mesoporous ZSM-5, the obtained Fe5Cu5/ME displayed the highest activity, which can be attributed to both the minimized nanoparticle size and the enhanced bimetallic interaction. The mesoporous ZSM-5 support used in this work was obtained from alkaline treatment, which led to a rough mesoporous surface. This surface sufficiently enhanced the dispersion and prohibited metal migration, therefore, preventing nanoparticle aggregation and enhancing the bimetallic interaction. The strategy of using mesoporous ZSM-5 obtained from alkaline treatment as a support is a reliable method for preparing multi-metallic catalysts with well-dispersed nanoparticles.

1 Introduction

Well-dispersed nanoparticles of metals and oxides have important applications as catalysts for the production of fuels and chemicals and for the reduction of environmental pollution.[1] High surface areas are important for these metal (oxide) nanoparticles since catalytic processes take place at the surface defects.[2] Therefore, supports, such as ZSM-5, SBA-15, Al_2O_3, are generally used to obtain nano-sized and thermally stable particles.[3] Furthermore, the use of active matrices is beneficial for the synergetic effect between metal and the support.

Bimetallic oxide catalysts can exhibit synergistic properties[4]. The use of two components can not only improve the metal dispersion and the interfacial structure, but also adjust the acidity, the durability and the selectivity.[2, 5] Bimetallic Fe-Cu, as one of the most important environmental catalysts, has been extensively studied in NO_x-SCR[6] as well as for removal of macromolecule effluent[7] and small molecular impurities[8]. The dispersion of bimetallic components and their strong metal-support interaction (SMSI)[2a] largely affect their catalytic properties. Supporting bimetallic components on ZSM-5 and mesoporous materials is an effective way to enhance the dispersion[9], but the conventional microporous zeolite support could easily lead to metal aggregation on the outer surface.[10] Ordered mesoporous materials support (SBA-15[11], MCM-41[12]) are limited due to their low hydrothermal stability and low resistance to acidity, which is not good for the adsorption of organic reactants[13].

Currently, varied assortment of top-down and bottom-up methods are available to obtain mesoporous zeolites[14]. The bottom-up method, which commonly necessitates the use of costly and commercially unavailable reactants as mesopore-inducing agents, has a low chance for industrialization[14,15]. As a comparison, the top-down method, such as desilication by alkaline treatment, is much more effective and scalable at an acceptable cost[14,16,17], and many studies have investigated their potential[18]. Recently, mesoporous zeolites have been used as monometal or bimetal supports, and show great performance[19].

The objective of this work is to study the influence of mesoporous ZSM-5 support, obtained from alkaline treatment, on the supported metal particle size and determine whether the synergetic effect of using bimetallic oxides can be enhanced. As iron/copper and H_2O_2 consist of the significant Fenton-like catalytic system to degrade organics[20], the phenol oxidation reaction is applied to evaluate the catalytic activity and the enhanced bimetallic effect. The structure-activity relationship was also analyzed based on comprehensive characterization.

2 Experimental

2.1 Chemicals and materials.

The chemicals used include silicon (IV) oxide (28 wt%), ethylamine (EA, 65 wt %), tetrapropyl ammonium bromide (TPABr), tetraethylorthosilicate (TEOS), tetrapropylammonium hydroxide (TPAOH), sodium hydroxide (NaOH), ammonium nitrate, ferric nitrate ($Fe(NO_3)_3$•$9H_2O$), cupric nitrate ($Cu(NO_3)_2$•$3H_2O$). All above materials were purchased in reagent grade and used as such.

Preparation of Microporous ZSM-5. Microporous ZSM-5 was synthesized hydrothermally with the assistance of active seeds from a gel with the molar ratio of $1SiO_2$: $0.0125Al_2O_3$: 0.15TPABr: 1EA: $17H_2O$. The active seeding gel was prepared from a gel with the molar ratio of 1TEOS: 0.36TPAOH: $19H_2O$ by a traditional hydrothermal synthesis route. Typically, the mixture of 15.4 ml TEOS and 16.5 ml TPAOH (1.14 M) was stirred at 308 K for 3 h followed by adding 33 ml distilled water and stirring for another 2 h. The obtained gel was then transferred to 80 ^oC water bath for hydrothermal treatment for 72 h. After cooling down, the obtained seeding gel was directly used for the synthesis of ZSM-5 zeolites without any treatment. The synthesis of ZSM-5 was conducted by the following procedure. First, 113.4 g TPABr was dissolved with 666.7 g silica solution and afterwards with a solution of 222.6 g EA (65 wt %). The mixture was aged at room temperature for 30 min under mechanical stirring followed by adding a solution of 20.12 g $AlCl_3$•$6H_2O$ and 450 g H_2O. The as-prepared active seeding gel was then added into the above ZSM-5 precursor. The gel was then introduced to the stainless steel autoclave (2000 ml, filled volume 1500 ml) with hydrothermal treatment at 443 K for 72 h. The resulting solid was filtered, washed, and dried overnight at 373 K. The as–synthesized zeolite was calcined in static air at 813 K for 6 h to remove the template. The resulting sample was denoted as MI.

Preparation of Mesoporous ZSM-5. Mesoporous ZSM-5 was obtained through individual alkaline treatment of sample MI in sodium hydroxide (NaOH, 0.3 M). The treatment was carried out in a round-bottomed flask in which the corresponding aqueous solution was stirred at 400 rpm and heated to 338 K. After the temperature of the solution was stable, a certain amount of MI was added, and the suspension was left to react for another 30 min. The ratio of solid weight to liquid volume ($m_{solid}/V_{solution}$) was 33 g L^{-1}. Afterwards, the treatment solution was quenched, and the suspension was filtered and washed with distilled water until reaching neutral pH. The resulting solid was dried overnight at 373 K after which calcination was performed at the conditions described above for MI. The resulting zeolite was brought into ammonium form via three consecutive exchanges in aqueous NH_4NO_3 at 348 K for 1.5 h. Finally, those samples were calcined in static air at 813 K for 4 h to ensure the obtained solid was in the proton form, denoted as ME. Molar ratios of Si/Al in samples are shown in Tables S2.

Preparation of Fe_xCu_y/ZSM-5. A series of Fe_xCu_y/ZSM-5 samples were prepared through the incipient wetness impregnation method, which used iron nitrate as the Fe source and cupric nitrate as the Cu source, where x and y represent the mass percentage content of iron and copper in synthetic gel, respectively, and x plus y equals 10. Amounts of Cu and Fe in synthetic gel and Fe_5Cu_5/ZSM-5 samples are shown in Table S1. Typically, for preparing sample Fe_5Cu_5/MI, 1 g sample of MI was added into 1 g aqueous cupric nitrate and iron nitrate solution containing 0.05 g Cu and 0.05 g Fe. The desired catalysts were obtained after drying overnight at 373 K followed by calcination in static air at 773 K for 3 h to decompose iron nitrate and cupric nitrate.

2.2 Catalytic testing

All catalyst evaluations were conducted in a 100 ml round-bottom flask equipped with a magnetic stirring bar. In a typical procedure, 20 mg catalyst, 50 ml phenol solution (1 g L^{-1}), and 10.76 ml H_2O_2 solution (0.69 M) were added together into the flask followed by maintaining at 50 ^oC for the appropriate time. The products were analyzed by liquid chromatography. The molar ratio of H_2O_2/Phenol was 14.

2.3 Characterization

Powder X-ray diffraction (XRD) patterns were recorded on a Rigaku Smartlab diffractometer using a nickel-filtered CuKα X-ray source at a scanning rate of 0.02^o over the range between 5° and 80°.

Transmission electron microscopy (TEM) images were taken on a Tecnai G2 20 S-twin instrument (FEI Company) with an acceleration voltage of 200 kV. The samples for TEM analysis were prepared by dipping the carbon-coated copper grids into the ethanol solutions of the samples and drying at ambient conditions.

Ar isotherms were measured in a Quantachrome autosorb-iQ2 gas adsorption analyzer at 87 K. Prior to the measurement, the samples were degassed in vacuum at 573 K for 8 h. The Brunauer-Emmett-Teller (BET) method was applied to calculate the total surface area (S_{BET}), while the t-plot method was used to discriminate between micro- and mesoporosity. In the t-plot, the reported mesopore surface area (S_{meso}) consists of contributions from the outer surface of the particles as well as mesopores and macropores.

H_2-TPR measurements were carried out with ChemBET Pulsar TPR/TPD equipment (Quantachrome, USA) to analyze the reducibility of the calcined catalysts. Prior to the reduction, the calcined sample (0.10 g) was placed in a quartz tube reactor in the interior of a controlled oven. The sample was flushed with high purity argon at 573 K for 1 h to remove water and other contaminants then cooled down to room temperature. A gas mixture containing 5 vol% H_2 in Ar was passed through the sample at a total flow rate of 30 ml min^{-1}. The temperature and detector signals were then continuously recorded while heating at 10 K min^{-1} up to 1173 K. A cooling trap was also placed between the sample and the detector for removal of released water formed during the reduction process.

3 Results and discussion

3.1 Material synthesis and characterization

The XRD patterns of the two matrices (MI and ME) used in this work are shown in Figure 1. The five characteristic diffraction peaks of MFI topology at 7.8°, 8.8°, 23.0°, 23,9°, and 24.4° clearly indicate the only phase detected is that of ZSM-5 (JCPDS: 44-0003). The relative crystallinity (RC) is defined as the ratio of the diffraction peak intensity with the highest peak intensity. MI has a much higher RC value compared with ME, 100% vs 46%, as the preparation of ME is a process of random desilication that not only generates a mesoporous system but also leads to the amorphous silicon species deposition and resulting decreased RC value.

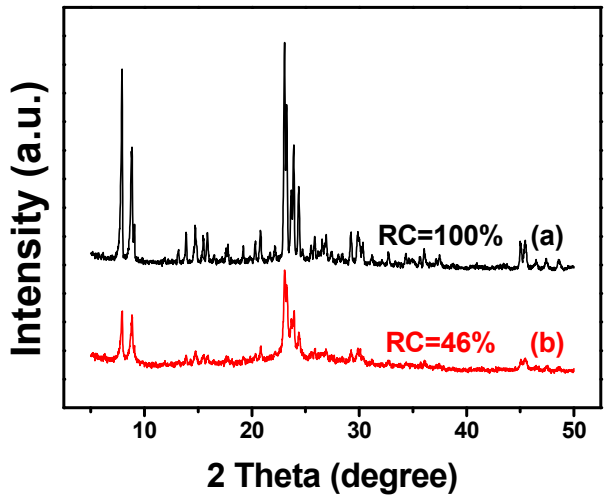

Fig. 1 XRD patterns of (a) MI (black line) and (b) (red line).

Table 1 Textural properties of MI and ME.

Sample	S_{micro} [a] [m^2g^{-1}]	S_{meso} [a] [m^2g^{-1}]	S_{BET} [b] [m^2g^{-1}]	V_{micro} [a] [cm^3g^{-1}]	V_{pore} [c] [cm^3g^{-1}]
MI	391	67	458	0.14	0.25
ME	204	152	358	0.08	0.61

[a] t-plot method [b] BET method [c] P/P_0=0.99.

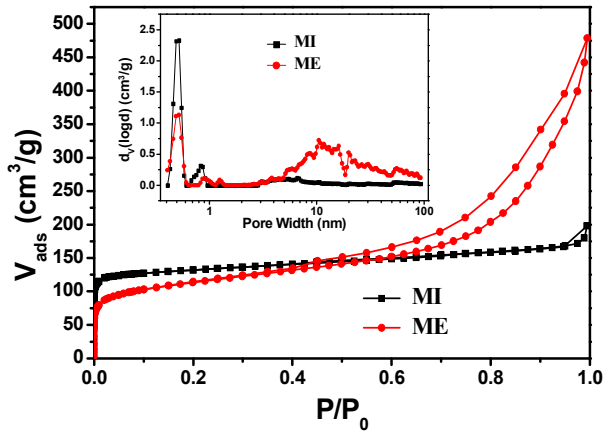

Fig. 2 Ar adsorption and desorption isotherms at 87 K and pore size distributions of MI and ME. The pore size distributions were determined by non-local density functional theory (NLDFT).

Figure 2 shows the Ar adsorption and desorption isotherms at 87 K with the pore size distributions of samples MI and ME presented as inset. The pore structure of ME extends from a micropore system to a hierarchical pore system with a mesopore distribution around 11 nm. More importantly, ME exhibits a much higher mesoporous surface area and pore volume compared with MI, as shown in Table 1.

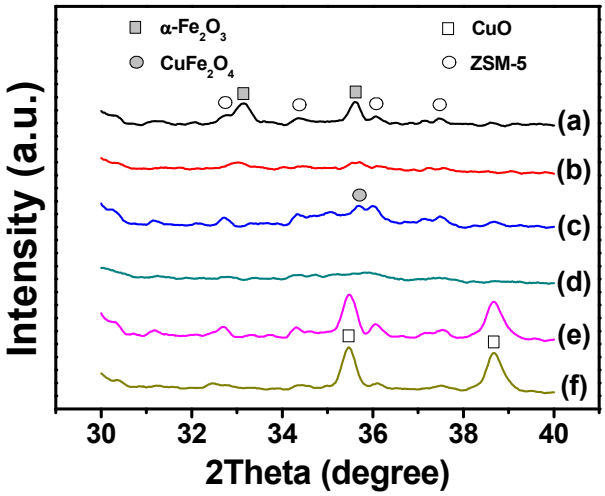

Fig. 3 XRD patterns of (a) Fe_{10}/MI, (b) Fe_{10}/ME, (c) Fe_5Cu_5/MI, (d) Fe_5Cu_5/ME, (e) Cu_{10}/MI, (f) Cu_{10}/ME.

Figure S1 shows the XRD patterns of Fe_xCu_y/ZSM-5. Besides the strong diffraction peaks of MFI topology, several new peaks appear between 30° and 40°. As shown in Figure 3, samples Fe_{10}/MI and Fe_{10}/ME exhibit α-Fe_2O_3 (JCPDS: 33-0664) diffraction peaks at 33.1°, 35.6°, 39.2°, with the diffraction peaks of α-Fe_2O_3 on Fe_{10}/ME much broader. The broader diffraction peaks observed for α-Fe_2O_3 in sample Fe_{10}/ME indicate that its particle size is much smaller than for sample Fe_{10}/MI, which is attributed to the increased mesoporous specific surface area. These results reveal that supporting transition metal oxides on mesoporous ZSM-5 can enhance the dispersion compared to that on microporous ZSM-5. Similarly, samples Cu_{10}/MI and Cu_{10}/ME with the same 10 wt% Cu loading exhibited the same trend regarding the metal particle size. As shown in Figure 3, samples Cu_{10}/MI and Cu_{10}/ME exhibited CuO (JCPDS: 45-0937) diffraction peaks at 35.6° and 38.6°. The half band widths of those two samples are clearly broader than those of the iron-containing samples, which is evidence that α-Fe_2O_3 possesses much larger particle size and lower dispersion than the supported CuO. The different extents of positive impacts by supports between iron and copper for minimizing the particle size is due to the difference in these metals' properties and the energy barriers for forming large particles. When supporting iron oxide on ME instead of MI, the introduction of rough mesoporous surface increased the energy barrier for iron oxide migration and aggregation and eventually prevented the agglomeration of α-Fe_2O_3. As the CuO supported on MI already has a good dispersion, the rough mesopore surface did not exhibit a stronger influence for decreasing CuO

particle size. Interestingly, upon supporting both Fe and Cu on MI or ME, diffraction peaks of both α-Fe_2O_3 and CuO were not detected. Instead, $CuFe_2O_4$ (JCPDS: 34-0425) peaks appeared for the FeCu bimetallic system. The presence of $CuFe_2O_4$ diffraction peaks is evidence for the strong bimetallic interaction which can lead to the formation of a spinel structure. Based on the observed effect of the rough mesoporous surface of ME, we speculate that sample Fe_5Cu_5/ME shown in Figure 3 also has the $CuFe_2O_4$ phase and with much smaller particle size.

Figure 4 and Figure S3 shows the TEM images of Fe_xCu_y/ZSM-5. The sample Fe_{10}/MI possesses much larger iron oxide particles agglomerated on the outer surface. In contrast, iron oxide supported on ME exhibits uniform size distribution and much smaller particle size, which is in line with the XRD analysis. However, samples Cu_{10}/MI and Cu_{10}/ME did not exhibit apparent differences in particle size according to the HRTEM images. In the case of sample Fe_5Cu_5/MI and Fe_5Cu_5/ME, both are well dispersed, and sample Fe_5Cu_5/ME present a much higher dispersion.

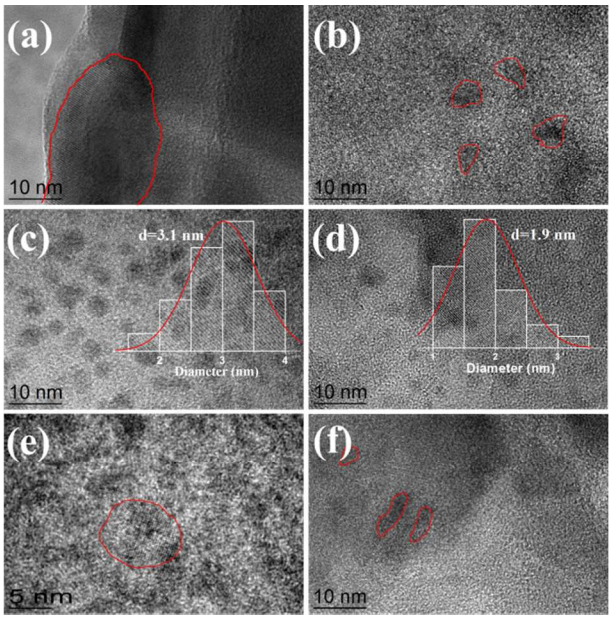

Fig. 4 HRTEM images of (a) Fe_{10}/MI, (b) Fe_{10}/ME, (c) Fe_5Cu_5/MI, (d) Fe_5Cu_5/ME, (e) Cu_{10}/MI, (f) Cu_{10}/ME.

To gain a better understanding of the strong interaction between iron and copper, H_2-TPR experiments were conducted. Figure 5 shows the H_2-TPR profiles of Fe_xCu_y/ZSM-5. For the iron-containing samples, the four H_2 consumption peaks are attributed to Fe^{3+} and Fe_2O_3 to $Fe^{(3-\delta)+}$ (α_1), with intermediate valence as that in Fe_3O_4, and then further reduction to Fe^{2+} (α_2). At higher temperature, the peaks represent partial reduction of Fe^{2+} to Fe^0 (α_3, α_4). For the copper-containing samples, the H_2 consumption peaks are attributed to Cu^{2+} and CuO reduction to Cu^+ and Cu_2O, then to Cu^+ reduction to Cu^0. As the copper species have a great variety of peaks[21], we attributed the copper peaks as β_1, β_2, β_3, β_4, β_5. According to the H_2-TPR profiles of the catalysts (shown in Figure 5), we compare sample Fe_{10}/MI and Fe_{10}/ME and it is observed that the peaks move to lower temperature. Combining with the original TEM images of those two samples, showing that iron oxides are larger for Fe_{10}/MI than Fe_{10}/ME, we conclude that the peak position of iron oxides depend on the particle size. The reduced particle size in Fe_{10}/ME facilitates the reduction of the iron oxides for the shortened reduced depth. When introducing copper to the catalyst, compared with Fe_{10}/ME and Fe_5Cu_5/ME, the introduction of copper makes the reduction peaks move to a higher temperature. Considering that sample Fe_5Cu_5/ME already has a great dispersion, smaller particle size would have moved the reduction peaks to the lower temperatures. However, peaks moving to higher temperature indicate a strong interaction between iron and copper, and this interaction dictates the reduction profile. On the other hand, when comparing sample Cu_{10}/MI and Cu_{10}/ME, the H_2 consumption peaks move to a higher temperature, contrary to the trends between Fe_{10}/MI and Fe_{10}/ME. That difference is attributed to copper being much easier to reduce for the same particle size. According to the H_2-TPR profiles, we attribute the peaks of Cu_{10}/ME moving to higher temperature to the strong interaction between copper and the support. When introducing iron to the catalyst, compared with Cu_{10}/ME and Fe_5Cu_5/ME, the introduction of iron makes the reduction peaks move to a lower temperature. This can be attributed to the weakened interaction between copper and the support, therefore, indicating the strong interaction between iron and copper. To summarize, H_2-TPR profiles allow us to conclude that iron and copper do strongly interact in the bimetallic samples and the strong interaction is a decisive factor to alter the TPR behavior.

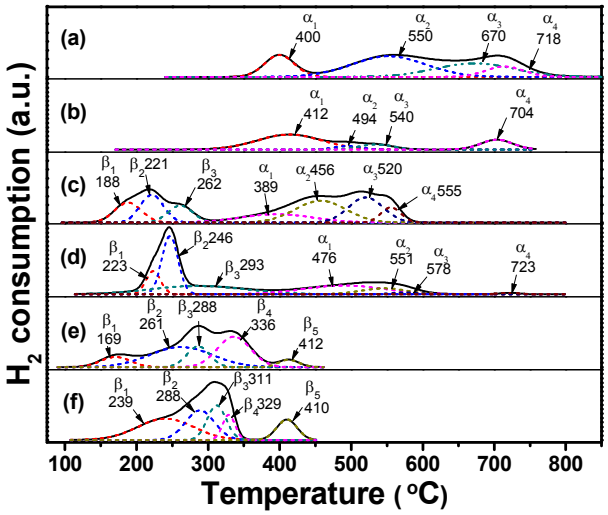

Fig. 5 H_2-TPR profiles of (a) Fe_{10}/MI, (b) Fe_{10}/ME, (c) Fe_5Cu_5/MI, (d) Fe_5Cu_5/ME, (e) Cu_{10}/MI, (f) Cu_{10}/ME.

To further investigate the nature of iron species, ^{57}Fe Mossbauer spectroscopic characterization was conducted. Figure 6 shows the ^{57}Fe Mossbauer spectra of Fe_5Cu_5/MI and Fe_5Cu_5/ME samples, with the hyperfine interaction parameters summarized in Table 2. In the case of sample Fe_5Cu_5/MI, three sextets were contained in the Mossbauer spectrum. The sextets with IS = 0.27 mm/s and 0.32 mm/s could be attributed to $CuFe_2O_4$-Site A and $CuFe_2O_4$-Site B, respectively.[22] Another sextet with ^{57}Fe Mossbauer parameters of IS = 0.36 mm/s and QS = -0.22 mm/s could be attributed to α-Fe_2O_3 with large

particle size.[23] Comparatively, sample Fe_5Cu_5/ME also has the $CuFe_2O_4$ and α-Fe_2O_3 phase according to Figure 6 and Table 2, but the nanoparticle size tends to move to the super paramagnetic direction. These results reveal that strong bimetallic interaction can result in the spinel phase generation.

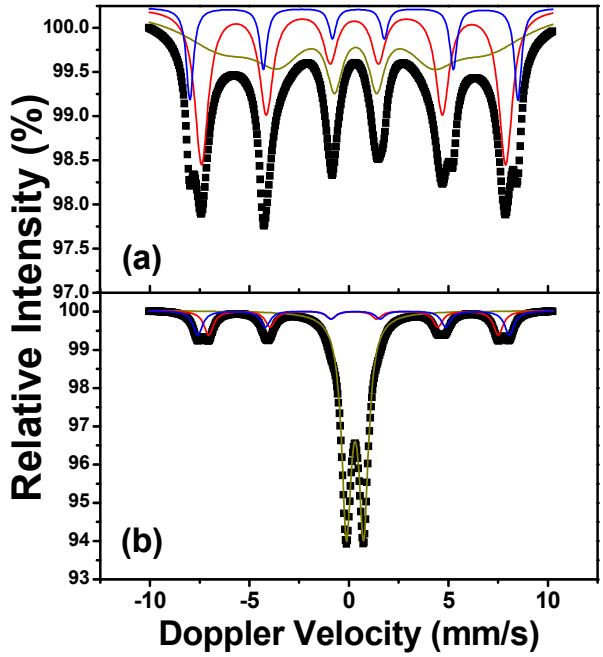

Fig. 6 ^{57}Fe Mossbauer spectroscopy of (a) Fe_5Cu_5/MI, (b) Fe_5Cu_5/ME.

Table 2 Hyperfine interaction parameters of ^{57}Fe Mossbauer spectra of Fe_5Cu_5/MI and Fe_5Cu_5/ME.

Sample	State	IS (mm/s)	QS (mm/s)	Magnitic Field (T)	RI (%)
Fe_5Cu_5/MI	$CuFe_2O_4$-Site A	0.26	-0.03	47.5	37.2
	$CuFe_2O_4$-Site B	0.32	0.04	41.5	51.4
	α-Fe_2O_3	0.36	-0.22	51.2	11.4
Fe_5Cu_5/ME	$CuFe_2O_4$-Site A	0.24	-0.02	45.1	15.9
	$CuFe_2O_4$-Site B	0.29	-0.10	48.6	15.8
	α-Fe_2O_3	0.31	0.86		68.4

3.2 Catalytic performance

Supported catalyst is composed of support and metallic oxides. The acidity of the support could influence the adsorption of the organic reactant. As shown in Figure S8, by supporting FeCu bimetallic oxides on mesoporous S-1, the obtained Fe_5Cu_5/meso-S-1 gave much lower initial phenol conversion, representing lower catalytic activity when compared with Fe_5Cu_5/ME. On the other hand, though supporting bimetallic oxides on ordered mesoporous materials can improve the catalytic performance (as shown in Figure S6), but the low hydrothermal stability limits its further fix-bed application. Consequently, mesoporous ZSM-5 was chosen as the bimetallic support because of its high hydrothermal stability and strong acidity.

Heterogeneous reactions take place at the surface defects and the synergetic effect can promote catalytic activities. Figure 7 and Figure S7 show the results of phenol conversion and H_2O_2 conversion in the presence of Fe_xCu_y/ZSM-5. There are clear differences in the initial catalytic activity among Fe_xCu_y/ZSM-5 catalysts. Compared with the initial phenol conversion catalyzed by Cu_{10}/MI, Cu_{10}/ME gave much higher initial phenol conversion, representing higher catalytic activity, which can be attributed to the minimized particle size of CuO on ME. Comparatively, the different activities of samples Fe_{10}/MI and Fe_{10}/ME can also be attributed to the nanoparticle size differences. In the case of sample Fe_5Cu_5/MI, the catalytic activity evenly matched with that of sample Cu_{10}/MI. However, when supported on ME, the difference between bimetallic Fe_5Cu_5/ZSM-5 and monometallic Cu_{10}/ZSM-5 became apparent. Though the catalytic activity of sample Fe_5Cu_5/ZSM-5 and Cu_{10}/ZSM-5 has a certain improvement due to the minimized nanoparticle size, sample Fe_5Cu_5/ME still has much higher activity, which can be attributed to the strong interaction between iron and copper. We conclude that the promoted activity of Fe_5Cu_5/ME can be attributed not only to the minimized particle size but also to the enhanced synergetic effect. In the presence of Fe_5Cu_5/ME and Fe_5Cu_5/MI, in the followed 6 h after quickly filtering the catalysts, the phenol continues to convert by 1% and 4% which is much lower than under the catalysts. That points out that the reaction proceeds mainly heterogeneous. The leaching of metal and the recycling performance are also conducted and shown in Table S4 and Figure S5. It can be seen that all six samples have some metal leaching and sample Fe_5Cu_5/ME maintains 80% phenol conversion with 4 times use. The decreased activity in recycling experiment may result from those metal leaching.

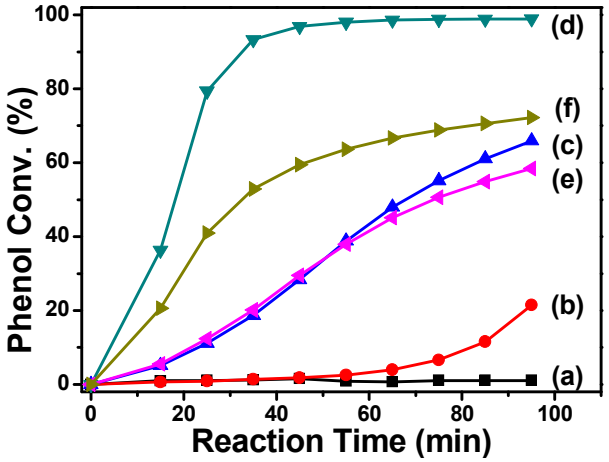

Fig. 7 Phenol conversion in the presence of (a) Fe_{10}/MI, (b) Fe_{10}/ME, (c) Fe_5Cu_5/MI, (d) Fe_5Cu_5/ME, (e) Cu_{10}/MI, (f) Cu_{10}/ME. Reaction conditions: Molar ratio: 14 H_2O_2: 1 phenol, 20 mg catalyst : 50 ml phenol (1 g/L), temperature is 323 K.

3.3 Discussion

Enhancing the bimetallic interaction is a key step for promoting the synergetic effect of the bimetallic catalysts. Minimizing the particle size and preparing high specific nanoparticle catalysts is the most direct way to promote the bimetal interaction, but this facile method requires the bimetal active sites being close enough. Until now, various techniques have been reported to decrease the particle size, and most of them are focused on the calcination atmosphere.[24] Using inert gas flow to remove the gas phase byproducts can be significantly beneficial for better metal dispersion and contribute to the quick removal rate of water, keeping the metal precursor in a solid form and thus benefitting the nano-sized crystal growth. However, the energy barrier for metal migration has not been changed, which means the high-temperature resistance of those as-prepared samples might be low.

In order to fundamentally increase the metal migration barrier, metal precursor was supported on mesoporous ZSM-5 obtained from alkaline treatment, which is a random desilication process and led to a rough surface (as shown in Figure 8). In the case of the sample prepared using conventional microporous ZSM-5 as a support, metal precursor is easier to migrate on the relatively smooth surface and tends to grow larger, which decreases the metal-support interaction. When the conventional ZSM-5 matrix was treated with alkaline solution (0.3 M NaOH), the random desilication led to the mesoporous ZSM-5. As shown in Figure 8, under alkaline aqueous conditions, Si-O-Si bonds are more susceptible to breaking, leading to a rough surface. The rough surface then can prohibit the migration of metal species and enhance the bimetallic interaction. XRD and TEM showed that particles on sample Fe_xCu_y/ME are indeed smaller than the particles on sample Fe_xCu_y/MI. H_2-TPR and the reaction evolution identified the enhanced strong metal interaction. These results confirm that increasing the energy barrier for migration of metal precursor can inhibit the aggregation of metal oxides and enhance the bimetallic effect. The new strategy to prepare multi-metallic catalysts by using mesoporous zeolite obtained through alkaline treatment is a general, robust and promising strategy to enhance the synergetic effect.

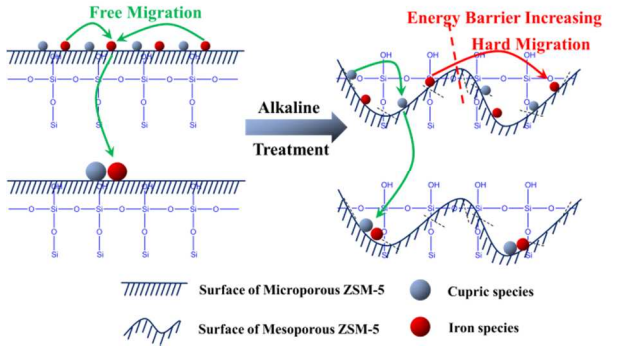

Fig. 8 Illustration of the enhanced bimetallic interaction by supporting Fe-Cu on ME.

4 Conclusions

In this work, mesoporous ZSM-5 (ME) obtained from alkaline treatment was used as a support for minimizing the nanoparticle size and enhancing the FeCu bimetallic interaction. In the present of mesoporous ZSM-5, the rough surface can prohibit the migration of metal species and thus can both decrease the particle size of single metal oxides and enhance the Fe-Cu interaction. The new strategy is a reliable method for multi-metallic catalyst preparation with well-dispersed nanoparticles.

Acknowledgements

This work was supported by the State Key Program of National Natural Science Foundation of China (grant no. 21236008).

Notes and references

[a] State Key Laboratory of Fine Chemicals, PSU-DUT Joint Center for Energy Research, School of Chemical Engineering, Dalian University of Technology, Dalian 116024, P. R. China.
[b] Mossbauer Effect Data Center, Dalian Institute of Chemical Physics, Chinese Academy of Sciences, Dalian, 116023, China.
[c] EMS Energy Institute, PSU-DUT Joint Center for Energy Research and Department of Energy & Mineral Engineering, Pennsylvania State University, University Park, Pennsylvania 16802, United States.

1 (a) J. R. A. Sietsma, J. D. Meeldijk, J. P. den Breejen, M. Versluijs-Helder, A. J. van Dillen, P. E. de Jongh and K. P. de Jong, Angew. Chem. Int. Ed., 2007, 46, 4547-4549. (b) N. J. Divins, I. Angurell, C. Escudero, V. Perez-Dieste and J. Llorca, Science, 2014, 346, 620-623. (c) J. Lu, B. Fu, M. C. Kung, G. Xiao, J. W. Elam, H. H. Kung and P. C. Stair, Science, 2012, 335, 1205-1208.
2 (a) J. Shi, Chem. Rev., 2013, 113, 2139-2181. (b) Q. Fu, W. X. Li, Y. Yao, H. Liu, H. Y. Su, D Ma, X. K. Gu, L. Chen, Z. Wang, H. Zhang, B. Wang, X. Bao, *Science*, 2010, **328**, 1141-1144.
3 (a) M. Cargnello, V. V. Doan-Nguyen, T. R. Gordon, R. E. Diaz, E. A. Stach, R. J. Gorte, P. Fornasiero and C. B. Murray, Science, 2013, 341, 771-773. (b) B. Li, M. Li, C. Yao, Y. Shi, D. Ye, J. Wu and D. Zhao, J. Mater. Chem., A, 2013, 1, 6742. (c) C. Dai, A. Zhang, L. Li, K. Hou, F. Ding, J. Li, D. Mu, C. Song, M. Liu and X. Guo, Chem. Mater., 2013, 25, 4197-4205.
4 (a) Y. Zhao, C. Ye, W. Liu, R. Chen and X. Jiang, Angew. Chem. Int. Ed., 2014, 53, 8127-8131. (b) H. Zhang, K. Kawashima, M. Okumura and N. Toshima, J. Mater. Chem., A, 2014, 2, 13498. (c) J. M. López, R. Arenal, B. Puértolas, Á. Mayoral, S. H. Taylor, B. Solsona and T. García, J. Catal., 2014, 317, 167-175. (d) P. J. Straney, L. E. Marbella, C. M. Andolina, N. T. Nuhfer and J. E. Millstone, J. Am. Chem. Soc., 2014, 136, 7873-7876. (e) B. Qiao, A. Wang, X. Yang, L. F. Allard, Z. Jiang, Y. Cui, J. Liu, J. Li and T. Zhang, Nat. Chem., 2011, 3, 634-641. (f) J. Lu, K. Low, Y. Lei, J. A. Libera, A. Nicholls, P. C. Stair and J. W. Elam, Nat. Commun., 2014, 5, 3264.
5 (a) B. Li, X. Hong, J. Lin, G. Hu, Q. Yu, Y. Wang, M. Luo, J. Lu, Appl. Surf. Sci., 2013, 280, 179-185. (b) X. Cui, J. Zhou, Z. Ye, H. Chen, L. Li, M. Ruan, J. Shi, J. Catal. 2010, 270, 310-317.
6 T. Zhang, J. Liu, D. Wang, Z. Zhao, Y. Wei, K. Cheng, G. Jiang, A. Duan, Appl. Catal., B, 2014, 148-149, 520-531.

7 B. Lai, Y. Zhang, Z. Chen, P. Yang, Y. Zhou, J. Wang, Appl. Catal., B, 2014, 144, 816-830.
8 H. Liu, M. Guo, Y. Zhang, Environ. Technol., 2014, 35, 917-924.
9 J. R. A. Sietsma, J. D. Meeldijk, M. Versluijs-Helder, A. Broersma, A. J. van Dillen, P. E. de Jongh and K. P. de Jong, Chem. Mater., 2008, 20, 2921.
10 C. H. Christensen, I. Schmidt, A. Carlsson, K. Johannsen and K. Herbst, J. Am. Chem. Soc., 2005, 127, 8098-8102.
11 (a) C. H. Christensen, I. Schmidt, A. Carlsson, K. Johannsen and K. Herbst, J. Am. Chem. Soc., 2005, 127, 8098-8102. (b) M. Mureddu, I. Ferino, A. Musinu, A. Ardu, E. Rombi, M. G. Cutrufello, P. Deiana, M. Fantauzzi and C. Cannas, J. Mater. Chem., A, 2014, 2, 19396-19406.
12 (a) M. Xia, M. Long, Y. Yang, C. Chen, W. Cai and B. Zhou, Appl. Catal., B, 2011, 110, 118-125. (b) A. I. Carrillo, E. Serrano, R. Luque and J. García-Martínez, Appl. Catal., A, 2013, 453, 383-390.
13 K. Na, C. Jo, J. Kim, K. Cho, J. Jung, Y. Seo, R. J. Messinger, B. F. Chmelka and R. Ryoo, Science, 2011, 333, 328-332.
14 D. Verboekend, G. Vilé and J. Pérez-Ramírez, Adv. Funct. Mater., 2012, 22, 916-928.
15 K. Möller and T. Bein, Chem. Soc. Rev., 2013, 42, 3689.
16 M. Milina, S. Mitchell, P. Crivelli, D. Cooke and J. Pérez-Ramírez, Nat. Commun., 2014, 5, 3922.
17 J. Pérez-Ramírez, S. Mitchell, D. Verboekend, M. Milina, Nina-Luisa Michels, F. Krumeich, N. Marti and M. Erdmann, ChemCatChem, 2011, 3, 1731.
18 D. Verboekend, J. Pérez-Ramírez, Catal. Sci. Technol. 2011, 1, 879.
19 (a) B. Puértolas, L. García-Andújar, T. García, M.V. Navarro, S. Mitchell, J. Pérez-Ramírez, Appl. Catal. B, 2014, 144, 161. (b) D.P. Serrano, J.M. Escola, L. Briones, S. Medina, A. Martinez. Fuel, 2015, 144, 287. (c) B.P. Ajayi, B. Rabindran Jermy, B. A. Abussaud, S. Al-Khattaf. J. Porous Mater., 2013, 20, 1257.
20 M. Hartmann, S. Kullmann, H. Keller, J. Mater. Chem., 2010, 20, 9002-9017.
21 (a) J. Sun, L. Zhang, C. Ge, C. Tang, L. Dong, Chin. J. Chem., 2014, 35, 1347-1358. (b) T. Zhang, J. Liu, D. Wang, Z. Zhao, Y. Wei, K. Cheng, G. Jiang and A. Duan, 2014, pp. 520-531.
22 Z. H. Xiao, S. H. Jin, J. H. Wang and C. H. Liang, Hyperfine Interact, 2013, 217, 151-156.
23 E. Manova, T. Tsoncheva, D. Paneva, M. Popova, N. Velinov, B. Kunev, K. Tenchev and I. Mitov, J. Solid State Chem., 2011, 184, 1153-1158.
24 (a) G. Prieto, J. Zečević, H. Friedrich, K. P. de Jong and P. E. de Jongh, Nat. Mater., 2012, 12, 34-39. (b) G. H. Torres, J. H. Bitter, C. B. Khare, M. Ruitenbeek, A. I. Dugulan and K. P. de Jong, Science, 2012, 335, 835-838. (c) T. van Haasterecht, T. W. van Deelen, K. P. de Jong and J. H. Bitter, Catal. Sci. Technol., 2014, 4, 2353-2366.